Applied Catalysis B: Environmental 284 (2021) 119687

Contents lists available at ScienceDirect

Applied Catalysis B: Environmental

journal homepage: www.elsevier.com/locate/apcatb

FeOx clusters decorated hcp Ni nanosheets as inverse electrocatalyst to stimulate excellent oxygen evolution performance

Wenxiu Yan [a,1], Yongli Shen [a,1], Chao An [a], Lina Li [b,*], Rui Si [b], Changhua An [a,*]

[a] Tianjin Key Laboratory of Organic Solar Cells and Photochemical Conversion, School of Chemistry and Chemical Engineering, Tianjin Key Laboratory of Advanced Functional Porous Materials, Institute for New Energy Materials & Low-Carbon Technologies, Tianjin University of Technology, Tianjin 300384, China
[b] Shanghai Synchrotron Radiation Facility, Shanghai Advanced Research Institute, Chinese Academy of Sciences, Shanghai 201204, China

ARTICLE INFO

Keywords:
Clusters
Crystal phase
Metal
Interface
Oxygen

ABSTRACT

Tuning the crystal phase of metals and constructing the metal-oxide interface provide a new way to improve oxygen evolution reaction (OER) kinetics. Herein, we developed a room-temperature plasma topology conversion of Fe^{3+} doping $Ni(OH)_2$ nanosheets to porous hcp Ni engineered by FeOx clusters. X-ray absorption fine spectra established that they were formed via Ni-O-Fe bonds. The metal oxide-metal interfaces with benign geometry and electronic structures enable it to be applied as efficient electrocatalyst, exhibiting overpotential of 226 mV at 10 mA cm^{-2}. In situ Raman spectra show that the interfacial action of FeOx cluster with Ni can stimulate the generation of active intermediate of γ-NiOOH, effectively promoting OER rate. DFT calculation further demonstrates the interaction accelerates desorption of O_2 molecules on the surfaces. This work provides a simple and robust strategy to synthesize oxide clusters engineering metastable metal nanocatalysts, offering new platform to explore efficient catalysts in various fields.

1. Introduction

With the development of social economy and human society, the consummation of traditional fossil fuels and increasing demand of energy has been a challenging issue [1]. The associated environmental problem during the utilization of energy stimulates the development of sustainable energy carrier. Electrochemical water-splitting to create hydrogen on the cathode and oxygen on the anode represents one of the promising strategies to convert intermittent renewable energies, such as sunlight, wind, and hydropower, into storable chemical fuels [2]. In this process, oxygen evolution reaction (OER) is a critical step due to the involvement of four-electron process with slow sluggish kinetics. The key is to explore efficient catalysts to accelerate reaction. Noble metal oxide such as IrO_2 or RuO_2 are often used as bench mark OER catalysts with overpotential of 350 mV at 10 mA cm^{-2} [3]. However, the earth-scarcity and high cost hinder their further practical applications.

Great strides have been made towards the exploit of cheap earth-abundant sources to achieve efficient OER electrocatalysts [4]. Typically, late-first row elements including Fe, Co, Ni with unique 3d electronic structures enable them to have suitable chemical bond strength with catalytic reaction intermediates and thus are appealing for heterogeneous catalytic/electrocatalytic reactions [5,6]. A variety of strategies including doping external elements [7], manufacturing porous structures [8], integrating carbon [9], and constructing heterostructures [10] have been used to tune their electronic structures. Despite the enormous progress in making OER catalysts, it is always desirable while challenging to produce optimal nanostructured candidates to decrease the overpotential further and increase the total electrode activity. Actually, besides the tuned parameters such as the size [11], shape [12], and the mentioned above, the stacking mode of metal atoms in different crystal phase gives rise to distinct crystal structure and electronic property [13], greatly influencing intrinsic catalytic property of metals. Typical phase control of noble metal nanoparticles with distinct catalytic properties has been made good progress from Zhang's group using wet-chemistry method [14–16]. Recently, Wang and coworkers used hcp-phase NiFe nanoparticles to modify N doped carbon by pyrolysis of related MOFs, revealing superior OER performance to fcc counterpart [17]. Hcp phase of PtNi multipods possesses a higher HER activity than fcc phase [18]. Liu et al. found that hcp phase Co nanocrystals exhibits higher performance than fcc Co in Fischer-Tropsch synthesis due to the lower CO dissociation on hcp Co [19]. Therefore, the realization of crystal-phase control of active electrocatalysts

* Corresponding authors.
E-mail addresses: lilina@sinap.ac.an (L. Li), anch@tjut.edu.cn (C. An).
[1] These authors contributed equally to this work.

https://doi.org/10.1016/j.apcatb.2020.119687
Received 23 August 2020; Received in revised form 14 October 2020; Accepted 21 October 2020
Available online 21 November 2020

provides a new path to optimize OER. Nevertheless, synthesis of metastable crystal phase of transition metal-based electrocatalyst is nontrivial, and the assembly of highly efficient electrocatalytic system is still challenging.

Herein, we put forward a facile CH_4 plasma strategy to convert Fe^{3+} doped $Ni(OH)_2$ nanosheets to porous hcp Ni nanosheets engineered by FeOx clusters (FeOx@hcp Ni). The constructed FeOx@hcp Ni has a confined metal−oxide interfaces with the combination of Ni-O-Fe bond, similar to the reverse catalysts in heterogeneous catalysis [20–22]. The strong interfacial interaction has been suggested to provide and stabilize highly active sites for molecular activation [23]. Such interfacial catalytic chemistry has rarely been noticed or utilized for electrocatalysis. We show that interaction of hcp Ni and FeOx could be significantly enhanced via metal-FeOx interfaces with beneficial geometry and electronic structures, realizing excellent OER performance with an overpotential of 226 mV at 10 $mAcm^{-2}$. In situ Raman tests show that the interfacial action of FeOx cluster with Ni can stimulate the generation of active intermediate of γ-NiOOH with $Ni^{3.6+}$, which is superior to β-NiOOH with primary Ni^{3+}. Meanwhile, DFT calculation further demonstrates the interaction accelerates

desorption of O_2 molecules on the surfaces. The present electrocatalysts of "metal oxide clusters on conductive metastable metal nanomaterials" may open a new way for the design of advanced electrocatalytic system for various applications.

2. Experimental

2.1. Chemicals

Carbon paper was purchased from Shanghai Hesen electric Co. Ltd. Ethanol, urea, potassium hydroxide, nickel (II) acetate tetrahydrate ($Ni(Ac)_2{\cdot}4H_2O$), and Iron (III) chloride hexahydrate ($FeCl_3{\cdot}6H_2O$) were purchased from Aladdin. Nafion (5 wt%) was purchased from Sigma-Aldrich. All the chemicals were used as received without further purification.

2.2. Synthesis of Fe doped $Ni(OH)_2$ nanosheets

Fe doped $Ni(OH)_2$ nanosheets was synthesized by a simple hydrothermal method. Briefly, 0.2488 g of $Ni(Ac)_2{\cdot}4H_2O$, 0.0124 g of $FeCl_3{\cdot}6H_2O$ and 0.24 g of urea were added into 30 mL of distilled water. After stirring 15 min, the resulting mixture was transferred into a 50 mL Teflon-lined stainless-steel autoclave and maintained at 150℃ for 6 h. The resulting materials was collected by centrifugation after being rinsed with water and ethanol several times. The bare $Ni(OH)_2$ nanosheets was also synthesized through a similar process without iron source.

2.3. Synthesis of porous FeOx@hcp Ni nanosheets

In a typical procedure, the quartz plate covered with Fe doped Ni $(OH)_2$ nanosheets was placed in the reaction chamber of a plasma-enhanced chemical vapor deposition (PECVD) system, followed by CH_4 plasma treatment at room temperature for 15 min with a base pressure of 20 Pa. The CH_4 flux was 30 sccm at a power of 400 W. After the reaction was complete, the sample color was changed from yellow-green to black. Similarly, porous hcp Ni nanosheets was also synthesized by reducing $Ni(OH)_2$ nanosheets.

2.4. Characterizations

X-ray diffraction (XRD) patterns were collected on a Rigaku Corporation UltimaIV diffractometer under Cu Kα radiation (40 kV, 40 mA, λ =1.5418 Å), recorded with 2θ ranging from 10° to 80°. The morphologies and microstructures of the catalysts were investigated by scanning electron microscope (SEM: ZEISS MERLIN Compact, Germany), transmission electronic microscope (TEM: Tecnai G2 Spirit TWIN, FEI), and high-resolution transmission electronic microscope (HRTEM) with FEG (Talos F200 X). X-ray photoelectronic spectroscopy (XPS) was performed on an ESCALAB 250Xi system. Raman spectra were collected on a Smart System HR Evolution (Horiba JobinYvon, France) using 532 nm laser source.

The XAFS at the Fe K (E° = 7112 eV) edge was gathered at 3.5 GeV in "top-up" mode with a constant current of 240 mA. The data were collected under fluorescence mode with a Lytle detector. The X-ray energy was calibrated with the absorption edge of pure Fe foil. Athena and Artemis codes were used to parse the data and fit the profiles. For the X-ray absorption near edge structure (XANES) part, the experimental absorption coefficients as function of energies μ(E) were managed by background subtraction and normalization procedures, and accounted as "normalized absorption". For the extended X-ray absorption fine structure (EXAFS) part, the Fourier transformed (FT) data in R space were analyzed by applying feff model to Fe-O and Fe-Ni (Fe-O-Ni) contributions. The passive electron factors S_0^2 were determined by fitting the experimental data on Fe foils and fixing the coordination number (CN) of Fe-Fe to be 8 + 6, and then fixed for further analysis of the measured samples. The parameters describing the electronic properties (e.g. correction to the photoelectron energy origin E°) and local structure environment including CN, bond distance (R) around the absorbing atoms were allowed to guess during the fit process. The fitted ranges for k and R spaces were set to be k = 3-10 $Å^{-1}$ with R = 1–3.4 Å (k^3 weighted).

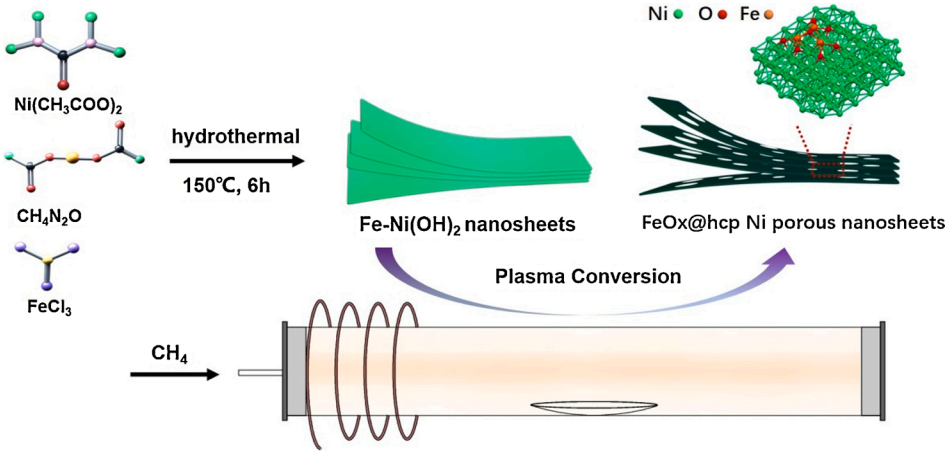

Fig. 1. A typical schematic illustration for the synthesis of FeOx@hcp Ni.

2.5. Electrocatalytic performance evaluation

The electrochemical tests were performed on a CHI 760E electrochemical workstation (CH Instruments, Inc., Shanghai) at room temperature with standard three-electrode system, where Hg/HgO electrode served as the reference electrode, graphite rod as the counter electrode, respectively. The working electrode was prepared as follows. 5.0 mg of electrocatalyst was dispersed in 1 mL ethanol and 80 μL Nafion solution (5 wt%, Sigma Aldrich) and sonicated 30 min. 10 μL of the catalyst ink was evenly coated onto the carbon paper with an area of 1 × 1 cm^2.

The OER evaluations were performed in aqueous electrolyte of 1 M KOH. The potential was converted to RHE by equation of $E_{RHE} = E_{Hg/HgO} + 0.098 + 0.059$ pH. The linear-sweep voltammograms (LSV) were scanned from 0 to 0.7 V versus saturated Hg/HgO at a rate of 10 mV/s. The ohmic potential drop loss that arises from the solution resistance has been corrected by iR compensation. Tafel plots were fitted to the equation of $\eta = a + b \log j$, where η is the overpotential, j is the cathodic current density, and b is the Tafel slope, respectively. Chronoamperometric tests were done at corresponding potential to deliver 20 mA/cm^2 for 20 h. Electrochemical impedance spectroscopy (EIS) was done in a frequency range of 0.01−100 kHz at a bias potential of 1.53 V (vs. RHE). The double-layer capacitance (C_{dl}) values were estimated by CV curves at different scan rates in the range of 0.2−0.3 V vs Hg/HgO. The C_{dl} is defined as $C_{dl} = \frac{dQ/dt}{dU/dt} = \frac{dJ}{dv}$, where Q represents the charge associated with movement of electrolyte ions and adsorption/desorption at the electrode-electrolyte interface, U is the applied potential, J is the corresponding current density, and v is the scan rate, respectively.

2.6. Computation models and methods

Spin-unrestricted calculations presented in this work were performed using the Vienna ab initio Simulation Package (VASP) code [24, 25]. The exchange-correlation function was described with generalized gradient approximation (GGA)-Perdew, Burke and Ernzerhof (PBE) function [26]. The electron wave function was expanded by means of plane waves with an energy cutoff of 400 eV. An hcp Ni (010) and Fe_3O_4 cut from bulk FeO anchored on hcp Ni (010) were constructed to represent the pure-Ni and FeOx@hcp Ni (010) inverse catalyst. Hcp Ni (010) was modeled by an eight-layer slab with a (3 × 4) unit cell and a vacuum region is set to be 30 Å between repeated slabs. A (2 × 2×1) k-point mesh was used for pure Ni and FeOx@hcp Ni (010). In our calculations, the bottom two layers of hcp Ni (010) and FeOx@hcp Ni (010) were fixed at the bulk positions and the top six layers together with the adsorbates are allowed to relax. Energies and forces were converged to within 10–5 eV and 0.02 eV/Å, respectively. Vibrational analysis for all the adsorbates has also been carried out, and the thermal corrections to Gibbs free energy for all adsorbates were achieved using VASPKIT program.

Gibbs free energy changes for the elementary reaction involved in OER were calculated as following:

$$\Delta G(OH) = G(OH^*) + 1/2(G(H_2) - kTln[H^+]) + eU - G(^*) - G(H_2O) \quad (1)$$

$$\Delta G(O) = G(O^*) + 1/2(G(H_2) - kTln[H^+]) + eU - G(OH^*) \quad (2)$$

$$\Delta G(OOH) = G(OOH^*) + 1/2(G(H_2) - kTln[H^+]) + eU - G(O^*) - G(H_2O) \quad (3)$$

$$\Delta G(O_2) = G(^*) + G(O_2) - G(O_2^*) \quad (4)$$

The desorption energy (E_{de}) of O_2 was calculated according to:

$$E_{de} = E(O_2) - E(catalyst) - E(O_2/catalyst) \quad (5)$$

where $E(O_2/catalyst)$, $E(catalyst)$ and $E(O_2)$ represent the energy of O_2 adsorption structure, energy of catalyst and the energy of the isolated O_2, respectively.

3. Results and discussion

3.1. Materials synthesis

Fig. 1 illustrates the formation process of FeOx@hcp Ni nanosheets. Fe doped $Ni(OH)_2$ nanosheets was firstly synthesized by a hydrothermal reaction. Then the as-obtained Fe doped $Ni(OH)_2$ was transformed into FeOx@hcp Ni under CH_4 plasma at room temperature. The material formation reaction can be formulated as follows.

$$CH_4 \xrightarrow{Plasma} *H + *CH_3 + *CH_2 + *C_2H_5 + *CH + etc. \quad (1)$$

$$Fe - Ni(OH)_2 \xrightarrow[\text{Room temperature}]{CH_4 \ Plasma} \text{FeOx@hcp} \quad \text{Ni} \quad (2)$$

$$Fe - Ni(OH)_2 \xrightarrow[400\ ^\circ C]{CH_4 \ Plasma} \text{FeOx@fcc} \quad \text{Ni} \quad (3)$$

In this process, the quantity of introducing Fe^{3+} has an impact on the microstructures of the final sample. The characterization of the precursors has been given in supporting information (Fig. S1). It is found that the excessive addition of iron source leads to the serious aggregation (Fig. S2). SEM images (Fig. S3) shows that the inheritance of morphology before and after plasma treatment maintained well.

3.2. Characterizations

Fig. 2a is XRD patterns of the samples converted from $Ni(OH)_2$ and Fe doped $Ni(OH)_2$. All the diffraction peaks can be indexed to the hcp Ni, consisting with the reported data [27]. For the obtained sample from conversion of Fe doped $Ni(OH)_2$, the shift of diffraction peaks to low angle show the certain interaction of Fe with Ni (Fig. S1). No signals of crystalline Fe species occur in the pattern, implying that it may exist in the form of amorphous clusters. SEM images (Fig. 2b, c) show that the thickness of nanosheets is about 9−10 nm. TEM image (Fig. 2d) of FeOx@hcp Ni reveals its rough surface with porous features, which can provide abundant active sites and facilitate electron transfer, intermediate adsorption and thus enhanced OER performance. The layer spacing of the nanosheets is ~1.8 nm (Fig. S4). Figs. S4c, S5 demonstrate that Fe atoms have merged into the lattice of $Ni(OH)_2$, resulting in the slight expansion of lattice spacing from 0.238 nm to 0.241 nm. Furthermore, HRTEM fringes (Figs. 2e-h) show the (010) and (002) planes of hcp Ni, demonstrating in situ conversion of $Ni(OH)_2$ results in the formation of nanopores in a process of the removal of hydroxyl radicals in a fast way [28]. We used the Brunauer–Emmett–Teller (BET) method to study the changes of specific surface area before and after plasma treatment. The specific surface area of the treated sample (104 m^2/g, FeOx@hcp Ni) is significantly higher than that over pristine

$Fe@Ni(OH)_2$ (38 m^2/g,) (Fig. S6). The diameter of the nanopores in $Fe@Ni(OH)_2$ is mainly in mesoporous scale, while the FeOx@hcp Ni has mesoporous and macroporous features. No iron-related lattices were observed, further revealing amorphous nature of iron species. The diffraction rings in SAED pattern (Fig. 2i) illustrate polycrystalline nature of the sample, which can be indexed to (002), (011) and (012) planes of hcp Ni. As given in Figs. 2j-m, S6, the energy dispersion spectrum (EDS) and element mapping of FeOx@hcp Ni indicates that Ni, Fe and O atoms are evenly distributed over the nanosheets, further proving that the sample is probably existed as FeOx@hcp Ni. Unfortunately, the strong magnetic property of the samples challenges the detail observation of surface FeOx clusters.

XANES of Fe K-edge of FeOx@hcp Ni was used (Fig. 3a) to further probe into the fine structure of FeOx@hcp Ni. In comparison with the reference Fe foils, Fe_2O_3, and Fe_3O_4, Fe edges over FeOx@hcp Ni have similar edge shape to that of Fe_3O_4 reference, indicating that the average oxidation state is close to Fe (III) state [29]. Fig. 3b gives EXAFS to detail the local coordination environment of Fe atoms. The spectrum gives two peaks with total Gaussian distribution at about 1.99 Å and 3.04 Å, which is different from the Fe foil. The EXAFS with the data-fitting in R space was to determine the short-range local coordination condition including distances and coordination number (CN) around the Fe atoms. On the basis of EXAFS fitting (Fig. 3c and Table S1), two strong peaks at 1.99 Å with CN of 4.9 and 3.04 Å with 4.7 were identified for the Fe-O and Ni-Fe bonds [30,31], respectively. The results are consistent with XPS and HRTEM analysis, confirming the presence of FeOx clusters. H_2-TPR over FeOx@hcp Ni and the mixture of Fe_2O_3 and Fe_3O_4 show two intense reduction peaks (Fig. 3d), corresponding to the reduction of Fe^{3+} and Fe^{2+}, respectively, showing that Fe is in the form of oxides [32,33]. However, the reduction peaks move to the low temperature region for the FeOx@hcp Ni due to the reduction of FeOx clusters interfered by interacting with Ni. H_2-TPR of NiO (Fig.S8) reveals the different reduction peak position from FeOx@hcp Ni, indicating that no NiO presented in the sample.

XPS was performed to investigate the surface composition and chemical states of the as-prepared samples. The survey spectrum of original Fe doped $Ni(OH)_2$ and the as-obtained FeOx@hcp Ni (Fig. S9) reveal the presence of O, Ni, Fe without other impurities. The high resolution Ni 2p spectra of pristine $Ni(OH)_2$ in Fig. 4a reveal the binding energies at 855.1 (Ni $2p_{3/2}$) and 872.8 eV (Ni $2p_{1/2}$) for Ni^{2+}, accompanying with two satellite peaks at 861.4 and 879.2 eV [34]. In Fe doped $Ni(OH)_2$, the binding energies of both Ni $2p_{3/2}$ and Ni $2p_{1/2}$ have positive shift of ~ 0.3 eV [35], suggesting the interaction of Fe^{3+} with Ni $(OH)_2$. After plasma treatment, as shown in Fig. 3b, the

main peaks of Ni 2p at 852.6 and 869.8 eV can be assigned to Ni $2p_{3/2}$ and Ni $2p_{1/2}$ of Ni^0 over the obtained hcp Ni, respectively [36]. The weak signals at 856.4 and 873.4 eV belonged to Ni $2p_{3/2}$ and Ni $2p_{1/2}$ of Ni^{2+} state with the satellite peaks at 860.9 and 879.1 eV, which is caused by inevitable oxidation during sample processing. The Ni 2p of FeOx@hcp Ni shows similar signals. However, the binding energy of Ni

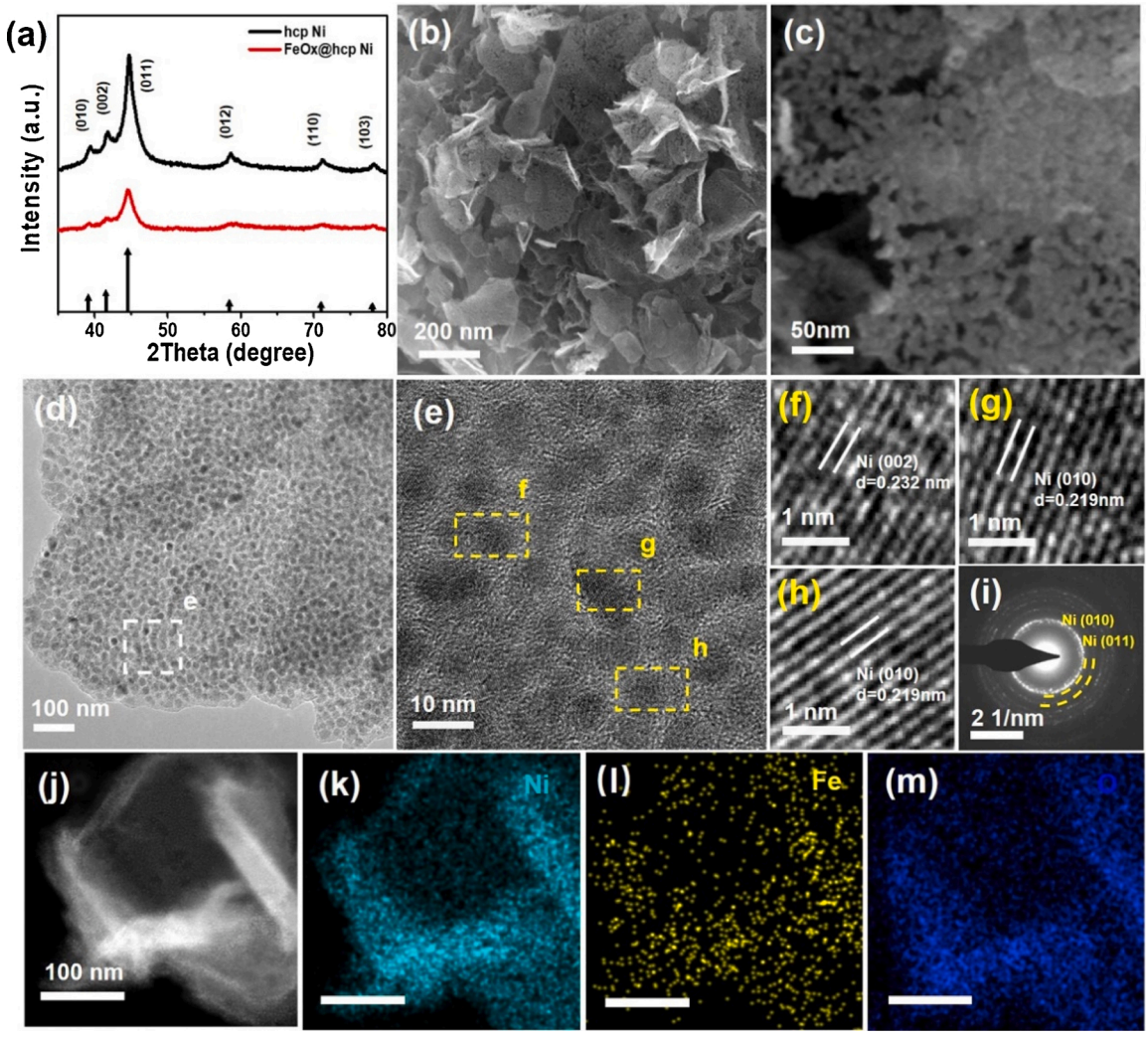

Fig. 2. Structure characterizations of FeOx@hcp Ni: (a) XRD patterns, (b-c) low and high magnified SEM images, (d-e) Low and high magnification TEM images, (f-h) HRTEM images, (i) SAED pattern,and (j-m) Elemental mapping images of Ni, Fe, and O.

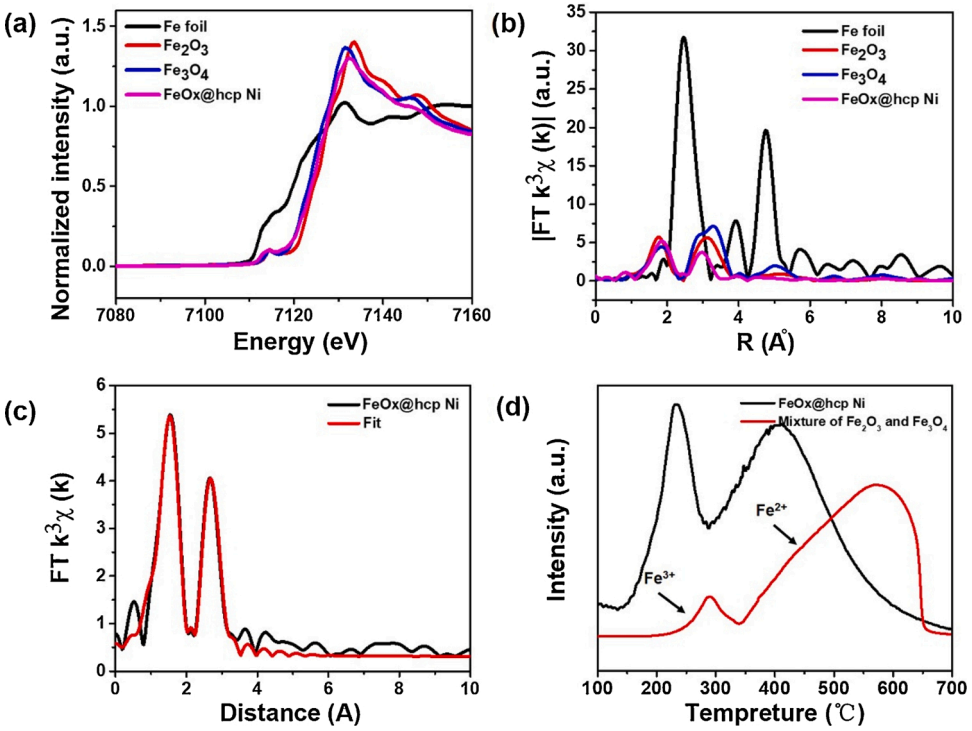

Fig. 3. (a) The normalized Fe-edge XANES spectra of different samples and references, (b) Fourier transform magnitudes of the experiment Fe K-edge EXAFS spectra of Fe foil, (c) Fourier-transformed magnitudes of Fe K-edge EXAFS spectra in R space for FeOx@hcp Ni, and (d) H_2-TPR profiles over a mixture of Fe_2O_3 and Fe_3O_4 and FeOx@hcp Ni.

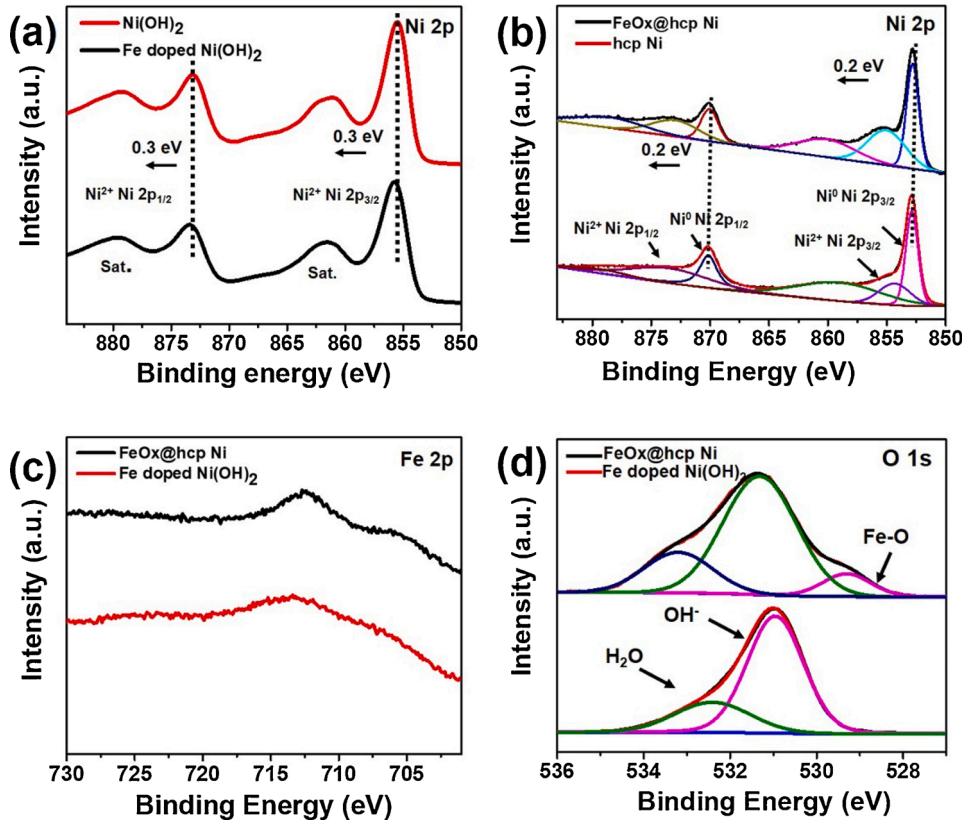

Fig. 4. XPS spectra of (a) Ni 2p of $Ni(OH)_2$ and Fe doped $Ni(OH)_2$, (b) Ni 2p of hcp Ni and FeOx@hcp Ni, (c) Fe 2p of FeOx@hcp Ni, Fe doped $Ni(OH)_2$, and (d) O 1s of Fe doped $Ni(OH)_2$ and FeOx@hcp Ni.

2p exhibits a shift of ~0.2 eV to the positive direction compared to single hcp Ni due to the electronic interaction between FeOx and hcp Ni. That is to say, the valence electrons can be transferred to FeOx clusters, leading to the improved valence of Ni. Fig. 4c gives binding energies of Fe 2p, showing that 712.3 and 725.2 eV correspond to the state of Fe^{3+} in the sample of Fe doped $Ni(OH)_2$ [37]. For FeOx@hcp Ni, the peaks have a negative shift of ~ 0.1 eV, implying that the valence state of Fe is descended slightly due to the acceptance of electrons from Ni. The results are consisting with the XAFS. The O 1s signal of 529.4 eV is for the newly formed FeOx clusters, showing the combination of iron and oxygen during the synthetic process (Fig. 4d) [38]. While the peaks at 531.1 eV and 532.8 eV are for the adsorbed water molecules and hydroxyl groups in Fe doped $Ni(OH)_2$, respectively.

3.3. Electrocatalytic OER performance

The electrocatalytic OER performances of the as-obtained FeOx@hcp Ni, hcp Ni, Fe doped $Ni(OH)_2$, $Ni(OH)_2$, and standard IrO_2 were evaluated at a scan rate of 10 mV s^{-1}. As shown in Fig. 5a, the Fe doped $Ni(OH)_2$ exhibits lower overpotential (317 mV) at 10 mA cm^{-2} compared to $Ni(OH)_2$ (349 mV), suggesting the incorporation of Fe promotes the catalytic performance. To attain a current density of 10 mA cm^{-2} and 100 mA cm^{-2}, porous single hcp Ni nanosheets requires an overpotential of 309 mV and 453 mV, respectively. Remarkably, FeOx@hcp Ni requires only 226 mV to realize current density of 10 mA cm^{-2} and 310 mV to achieve 100 mA cm^{-2}, respectively, demonstrating substantial improvement in OER activity compared with $Ni(OH)_2$ (100 mA cm^{-2} at 670 mV). Furthermore, the OER performance over FeOx@hcp Ni is also superior to fcc Ni supported FeOx (255 mV) at 10 mA cm^{-2} (Fig. S12b). The Tafel slope over FeOx@hcp Ni is determined to be 68.1 mV dec^{-1}, which is much less than that of FeOx@fcc Ni (85.1 mV dec^{-1}) (Fig. S12c), showing better kinetic for OER on hcp phase. Nyquist plots (Fig. S12d) show that FeOx@hcp Ni has higher conductivity. The distinction of OER activity between two samples mainly from the different phase of Ni. Hcp phase Ni nanosheets has different crystal structures and electronic property from fcc phase Ni, resulting in the remarkable electronic interaction with FeOx clusters. The activity is also better than those of most reported similar examples (Table S2). Fig. 5c is Tafel plots of the corresponding polarization curves. The Tafel slopes over FeOx@hcp Ni (68.1 mV dec^{-1}) is much less than that of hcp Ni (88.5 mV dec^{-1}), Fe doped $Ni(OH)_2$ (98.4 mV dec^{-1}), $Ni(OH)_2$ (146.5 mV dec^{-1}), and IrO_2 (93.6 mV dec^{-1}). The lowest Tafel slope value of FeOx@hcp Ni indicates the higher catalytic kinetics [39]. To further illustrate the superior catalytic performance, electrochemical impedance spectroscopy (EIS) measurement was carried out. Nyquist plots (Fig. 5d) show that FeOx@hcp Ni (3.5 Ω) has the highest conductivity, suggesting its good electron transfer capacity. Charge transfer resistance (R_{ct}) is also reduced with the introduction of Fe into $Ni(OH)_2$, implying that Fe doped $Ni(OH)_2$ (13.5 Ω) has better electron transportability than bare $Ni(OH)_2$ (35.7 Ω).

In general, the electrochemical active surface area (ECSA) is closely related to the activity of each catalyst, which can be estimated by double-layer capacitance (C_{dl}) from cyclic voltammetry (CV, Fig. S13) in the non-faradic region [40]. As depicted in Fig. 5e, the C_{dl} values of FeOx@hcp Ni, Fe doped $Ni(OH)_2$, hcp Ni, $Ni(OH)_2$ is 8.4, 5.4, 5.1 and 2.8 m F cm^{-2}, respectively, demonstrating that FeOx@hcp Ni has the highest ECSA. The stability is also an important parameter for catalysts. As illustrated in Fig. 5f, the polarization curve of FeOx@hcp Ni exhibits negligible loss after testing 2500 cycles, showing good stability of the catalyst. Furthermore, the FeOx@hcp Ni displays excellent durability at current density of 20 mA cm^{-2} after 20 h, retaining the original morphology, crystal phase (Fig. S15), and porous structure (Fig.S14).

3.4. Analysis of OER mechanism

In order to gain better understanding of the dominant phase in the reaction, we analyzed the interfacial active phase of the catalyst in the electrochemical process by operando Raman spectroscopy [41]. Fig. 6a shows a series of Raman spectra over FeOx@hcp Ni at selected applied potentials vs Hg/HgO. The electrode surface undergoes phase transformation at the potential of 0−0.65 V. As the potential goes at 0.4 V, the signals of γ-NiOOH with $Ni^{3.6+}$ (it is superior to β-NiOOH with primary Ni^{3+} [41]) appear at 475 cm^{-1} and 555 cm^{-1}, similar to the reported NiOOH as key intermediate of OER [42–44].

The computational results show that the hcp Ni catalyst is actually conducive to the formation of O_2 from the electrochemical point of view [45]. All the elementary reactions involving proton-electron pair demonstrate that the formation of *OOH is the potential-limiting step of

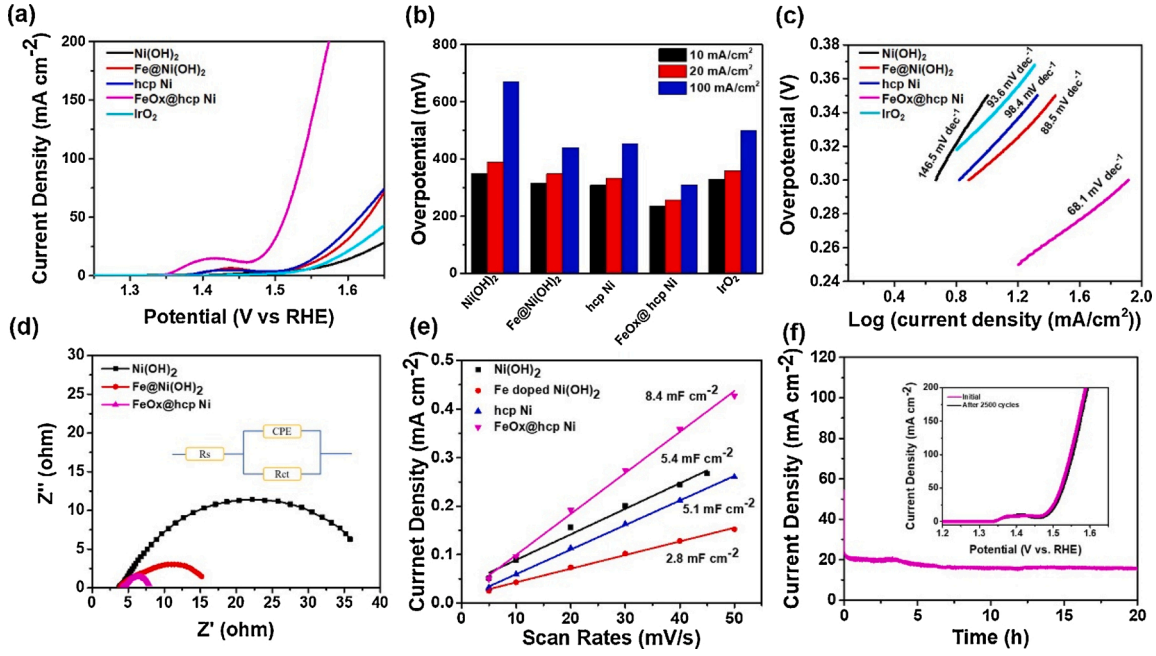

Fig. 5. Electrocatalytic OER evaluations. (a) Polarization curves, (b) the overpotentials over various electrocatalysts at 10, 50, and 100 mA cm^{-2}, (c) the corresponding Tafel plots, (d) Nyquist plots at 1.53 V *vs* RHE, (e) the plot of capacitive currents *vs* scan rates at 1.15 V vs RHE, and (f) The Chrono-potentiometric curves of OER test at 20 mA cm^{-2}. The inset is polarization curves of FeOx@hcp Ni for the durability test after 2500 CV cycles.

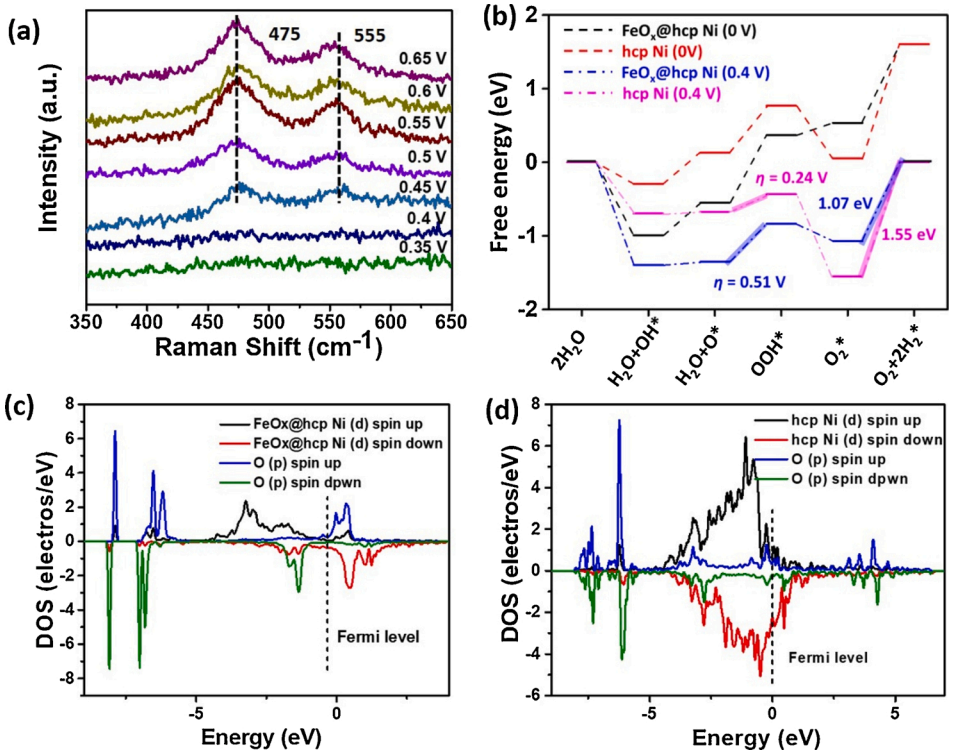

Fig. 6. (a) In operando Raman spectra of the FeOx@hcp Ni collected in the different potential range, (b) Free-energy diagram for oxygen evolution over hcp Ni (010) and FeOx@hcp Ni (010). Dash and dash-dot lines represent reactions at U = 0 V and U = 0.40 V (equilibrium potential at PH = 14), respectively. Potential-limiting step are shown in bold lines. (c, d) The local density of states (DOS) of FeOx@hcp Ni and hcp Ni for adsorbed oxygen molecules.

the OER (Fig. S17). If the O_2 desorption process (a thermochemical reaction) is not considered, the theoretical overpotentials for the hcp Ni (010) and FeOx@hcp Ni (010) catalyst are 0.24 V and 0.51 V, respectively. However, when O_2 formed, it exists on the catalyst surface in an adsorbed state. Therefore, there must be an O_2 desorption process in the whole reaction, which should also be considered. From Fig. 6b it can be speculated that hcp Ni (010) catalyst has strong adsorption to O_2, thus it is relatively difficult for O_2 to desorb from the surface of hcp Ni (010). The desorption free energy for O_2 molecules on hcp Ni (010) and FeOx@hcp Ni (010) catalyst are estimated to be 1.55 eV and 1.07 eV, respectively, which is obviously higher than the theoretical overpotentials of those two catalysts. Moreover, It is obvious from the DOS diagram (Fig. 6c, d) that the oxygen molecules produced by H_2O decomposition can be effectively adsorbed on the surface of the hcp Ni (010) and FeOx@hcp Ni (010) catalysts. However, on the surface of hcp Ni (010) catalyst, there are obviously more oxygen p bands and d bands with similar energy and shape. This is to say that O_2 has stronger interaction with the hcp Ni (010) catalyst, which is the reason why O_2 has higher desorption energy on the surface of the hcp Ni (010) catalyst. Therefore, the desorption process of O_2 is probably the key factor affecting the catalytic activity of hcp Ni (010) and FeOx@hcp Ni (010) towards OER.

4. Conclusion

In summary, for the first time, we have synthesized FeOx@hcp Ni inverse electrocatalysts via a simple room temperature plasma process. The detail structure from XAFS, HRTEM, and H_2-TPR confirmed the presence of FeOx clusters-Ni interfaces with a bond of Ni-O-Fe. The interfacial interaction between FeOx clusters and hcp Ni endows the catalysts with beneficial geometry and electronic structures, facilitating the OER. It exhibits outstanding OER performance with 226 mV overpotential at 10 mA cm^{-2}, which is better than many reported data. The DFT calculation shows when the FeOx cluster is introduced, the desorption process of oxygen is optimized and overpotential is further reduced in comparison with single hcp Ni. In situ Raman spectra demonstrate that the formation of γ-NiOOH intermediate is beneficial for OER. This work presents a general and facile method to design unusual metal nanocatalysts and related hybrid catalytic system. We believe that a variety of key catalytic reactions can be enhanced over the metastable-phase model catalysts, promoting the establishment of structure-property relationship.

CRediT authorship contribution statement

Wenxiu Yan: Conceptualization, Methodology, Investigation, Data curation, Writing - original draft. **Yongli Shen:** Formal analysis, Software. **Chao An:** Investigation, Writing - original draft. **Lina Li:** Resources, Data curation. **Rui Si:** Resources, Data curation. **Changhua An:** Conceptualization, Methodology, Supervision, Project administration, Funding acquisition.

Declaration of Competing Interest

The authors declare that they have no known competing financial interests or personal relationships that could have appeared to influence the work reported in this paper.

Acknowledgments

We thank the staff of the 11B beamline at the Shanghai Synchrotron Radiation Facility (SSRF) for data collection. This work has been supported by the project of National Natural Science Foundation of China (21771137, 21773288, U1932119), National Key Basic Research Program of China (2017YFA040340), Natural Science Foundation of Tianjin City (18JCJQJC47700), and the Training Project of Innovation Team of Colleges and Universities in Tianjin (TD13-5020). This work was also

supported by shanghai large scientific facilities center.

Appendix A. Supplementary data

Supplementary material related to this article can be found, in the online version, at doi:https://doi.org/10.1016/j.apcatb.2020.119687.

References

[1] L. Hu, X. Zeng, X. Wei, H. Wang, Y. Wu, W. Gu, L. Shi, C. Zhu, Interface engineering for enhancing electrocatalytic oxygen evolution of NiFe LDH/NiTe heterostructures, Appl. Catal. B: Environ. 273 (2020) 119014, https://doi.org/10.1016/j.apcatb.2020.119014.

[2] C. Tan, X. Cao, X. Wu, Q. He, J. Yang, X. Zhang, J. Chen, W. Zhao, S. Han, G. H. Nam, M. Sindoro, H. Zhang, Recent advances in ultrathin two-dimensional nanomaterials, Chem. Rev. 117 (2017) 6225–6331, https://doi.org/10.1021/acs.chemrev.6b00558.

[3] H. Jin, C. Guo, X. Liu, J. Liu, A. Vasileff, Y. Jiao, Y. Zheng, S.H. Qiao, Emerging two-dimensional nanomaterials for electrocatalysis, Chem. Rev. 118 (2018) 6337–6408, https://doi.org/10.1021/acs.chemrev.7b00689.

[4] Q. Shi, C. Zhu, D. Du, Y. Lin, Robust noble metal-based electrocatalysts for oxygen evolution reaction, Chem. Soc. Rev. 48 (2019) 3181–3192, https://doi.org/10.1039/C8CS00671G.

[5] M. Favaro, W.S. Drisdell, M.A. Marcus, J.M. Gregoire, E.J. Crumlin, J.A. Haber, J. Yano, An operando investigation of (Ni-Fe-Co-Ce)Ox system as highly efficient electrocatalyst for oxygen evolution reaction, ACS Catal. 7 (2017) 1248–1258, https://doi.org/10.1021/acscatal.6b03126.

[6] B. Wang, C. Tang, H.F. Wang, X. Chen, R. Cao, Q. Zhang, A nanosized CoNi hydroxide@hydroxysulfide core–shell heterostructure for enhanced oxygen evolution, Adv. Mater. 31 (2019) 1805658, https://doi.org/10.1002/adma.201805658.

[7] Y. Tang, Q. Liu, L. Dong, H.B. Wu, X.Y. Yu, Activating the hydrogen evolution and overall water splitting performance of NiFe LDH by cation doping and plasma reduction, Appl. Catal. B: Environ. 266 (2020) 118627, https://doi.org/10.1016/j.apcatb.2020.118627.

[8] J.H. Kim, D.H. Youn, K. Kawashima, J. Lin, H. Lim, C.B. Mullins, Manufacturing porous structure, Appl. Catal. B: Environ. 225 (2018) 1–7, https://doi.org/10.1016/j.apcatb.2017.11.053.

[9] H. Lei, Z. Wang, F. Yang, X. Huang, J. Liu, Y. Liang, J. Xie, M.S. Javed, X. Lu, S. Tan, W. Mai, NiFe nanoparticles embedded N-doped carbon nanotubes as high-efficient electrocatalysts for wearable solid-state Zn-air batteries, Nano Energy 68 (2020) 104293, https://doi.org/10.1016/j.nanoen.2019.104293.

[10] Y. Jia, L. Zhang, H. Chen, B. Wang, J. Zhou, M.T. Soo, M. Hong, X. Yan, G. Qian, J. Zou, A. Du, X. Yao, A heterostructure coupling of exfoliated Ni–Fe hydroxide nanosheet and defective graphene as a bifunctional electrocatalyst for Overall Water splitting, Adv. Mater. 29 (2017), 1700017, https://doi.org/10.1002/adma.201700017.

[11] C. Roy, B. Sebok, S.B. Scott, E.M. Fiordaliso, J.E. Sorrensen, A. Bodin, D. B. Trimarco, C.D. Damsgaard, P.C.K. Vesborg, O. Hansen, I.E.L. Stephens, J. Kibsgaard, I. Chorkendorff, Impact of nanoparticle size and lattice oxygen on water oxidation on $NiFeO_xH_y$, Nat. Catal. 1 (2018) 820–829, https://doi.org/10.1038/s41929-018-0170-x.

[12] Y. Chen, L. Shen, C. Wang, S. Feng, N. Zhang, S. Xiang, T. Feng, M. Yang, K. Zhang, B. Yang, Utilizing in-situ polymerization of pyrrole to fabricate composited hollow nanospindles for boosting oxygen evolution reaction, Appl. Catal. B: Environ. 274 (2020) 119112, https://doi.org/10.1016/j.apcatb.2020.119112.

[13] Y. Wang, M. Qiao, Y. Li, S. Wang, Tuning surface electronic configuration of NiFe LDHs nanosheets by introducing cation vacancies (Fe or Ni) as highly efficient electrocatalysts for oxygen evolution reaction, Small 14 (2018) 1800136, https://doi.org/10.1002/smll.201800136.

[14] X. Huang, H. Li, S. Li, S. Wu, F. Boey, J. Ma, H, Z, Synthesis of gold square-like plates from ultrathin gold square sheets: the evolution of structure phase and shape, Angew. Chem. Int. Ed. 50 (2011) 12245–12248, https://doi.org/10.1002/anie.201105850.

[15] Y. Chen, Z. Fan, Z. Luo, X. Liu, Z. Lai, B. Li, Y. Zong, L. Gu, H. Zhang, High-yield synthesis of crystal-phase-heterostructure 4H/fcc Au@Pd core–shell nanorods for electrocatalytic ethanol oxidation, Adv. Mater. 29 (2017) 1701331, https://doi.org/10.1002/adma.201701331.

[16] Q. Lu, A.L. Wang, Y.G, W. Hao, H. Cheng, J. Chen, B. Li, N. Chen, J. Luo, S. Li, L. Gu, H. Zhang, Crystal phase-based epitaxial growth of hybrid noble metal nanostructures on 4H/fcc Au nanowires, Nat. Chem. 10 (2018) 456–461, https://doi.org/10.1038/s41557-018-0012-0.

[17] C. Wang, H. Yang, Y. Zhang, Q. Wang, NiFe alloy nanoparticle with hexagonal close-packed crystal structure stimulates superior oxygen evolution reaction electrocatalytic activity, Angew Chem. Int. Ed. 58 (2019) 6099–6103, https://doi.org/10.1002/anie.201902446.

[18] Z. Cao, Q. Chen, J. Zhang, H. Li, Y. Jiang, S. Shen, G. Fu, B. Lu, Z. Xie, L. Zhang, Platinum-nickel alloy excavated nano-multipods with hexagonal close-packed structure and superior activity towards hydrogen evolution reaction, Nat. Commun. 8 (2017) 15131, https://doi.org/10.1038/ncomms15131.

[19] J.X. Liu, H.Y. Su, D.P. Sun, B.Y. Zhang, W.X. Li, Crystallographic dependence of CO activation on cobalt catalysts, J. Am. Chem. Soc. 135 (2013) 16284–16287, https://doi.org/10.1021/ja408521w.

[20] X. Guo, Q. Fu, Y. Ning, M. Wei, M. Li, S. Zhang, Z. Jiang, X. Bao, Ferrous centers confined on core−shell nanostructures for low temperature CO oxidation, J. Am. Chem. Soc. 134 (2012) 12350–12353, https://doi.org/10.1021/ja3038883.

[21] H. Yan, C. Yang, W.P. Shao, L.H. Cai, W.W. Wang, Z. Jin, C.J. Jia, Construction of stabilized bulk-nano interfaces for highly promoted inverse CeO_2 /Cu catalyst, Nat. Commun. 10 (2019) 3470, https://doi.org/10.1038/s41467-019-11407-2.

[22] J. Granciani, K. Mudiyanselage, F. Xu, A.E. Baber, J. Evans, S.D. Senanayake, D. J. Stacchiola, P. Liu, J. Hrbek, J.F. Sanz, J.A. Rodriguez, Highly active copper-ceria-titania catalysts for methanol synthesis from CO_2, Science 345 (2014) 546–551, https://doi.org/10.1126/science.1253057.

[23] P. Xiong, X. Zhang, H. Wan, S. Wang, Y. Zhao, J. Zhang, D. Zhou, W. Gao, R. Ma, T. Sasaki, G. Wang, Interface modulation of two-dimensional superlattices for efficient overall water splitting, Nano Lett. 19 (2019) 4518–4526, https://doi.org/10.1021/acs.nanolett.9b01329.

[24] G. Kresse, J. Furthmuller, Efficient iterative schemes for ab initio total-energy calculations using a plane-wave basis set, Phys. Rev. B 54 (1996) 11169–11186, https://doi.org/10.1103/PhysRevB.54.11169.

[25] G. Kresse, J. Furthmuller, Efficiency of ab-initio total energy calculations for metals and semiconductors using a plane-wave basis set, J. Comput. Mater. Sci. 6 (1996) 15–50, https://doi.org/10.1016/0927-0256(96)00008-0.

[26] J.P. Perdew, K. Burke, M. Ernzerhof, Generalized gradient approximation made simple, Phys. Rev. Lett. 77 (1996) 3868, https://doi.org/10.1103/PhysRevLett.781396.

[27] Q. Shao, Y. Wang, S. Yang, K. Lu, Y. Zhang, C. Tang, J. Song, Y. F41ng, L. Xiong, Y. Peng, Y. Li, H.L. Xin, X. Huang, Stabilizing and activating metastable nickel nanocrystals for highly efficient hydrogen evolution electrocatalysis, ACS Nano 12 (2018) 11625–11631, https://doi.org/10.1021/acsnano.8b06896.

[28] G. Liu, D. He, R. Yao, Y. Zhao, J. Li, Amorphous NiFeB nanoparticles realizing highly active and stable oxygen evolving reaction for water splitting, Nano Res. 11 (2017) 1664–1675, https://doi.org/10.1007/s12274-017-1783-0.

[29] W. Ren, X. Tan, W. Yang, C. Jia, S. Xu, K. Wang, S.C. Smith, C. Zhao, Isolated diatomic Ni-Fe metal–nitrogen sites for synergistic electroreduction of CO_2, Angew. Chem. Int. Ed. 58 (2019) 1–6, https://doi.org/10.1002/ange.201901575.

[30] M. Ma, A. Kumar, D. Wang, Y. Wang, Y. Jia, Y. Zhang, G. Zhang, Z. Yan, X. Sun, Boosting the bifunctional oxygen electrocatalytic performance of atomically dispersed Fe site via atomic Ni neighboring, Appl. Catal. B: Environ. 274 (2020) 119091, https://doi.org/10.1016/j.apcatb.2020.119091.

[31] B.H.R. Suryanto, Y. Wang, R.K. Hocking, W. Adammson, C. Zhao, Overall electrochemical splitting of water at the heterogeneous interface of nickel and iron oxide, Nat. Commun. 10 (2019) 5599, https://doi.org/10.1038/s41467-019-13415-8.

[32] A. Gervasini, C. Messi, P. Carniti, A. Ponti, N. Ravasio, F. Zaccheria, Insight into the properties of Fe oxide present in high concentrations on mesoporous silica, J. Catal. 262 (2009) 224–234, https://doi.org/10.1016/j.jcat.2008.12.016.

[33] W.W. Wang, W.Z. Yu, P.P. Du, H. Xu, Z. Jin, R. Si, C. Ma, S. Shi, C.J. Jia, C.H. Yan, Crystal plane effect of ceria on supported copper oxide cluster catalyst for CO oxidation: importance of metal−support interaction, ACS Catal. 7 (2017) 1313–1329, https://doi.org/10.1021/acscatal.6b03234.

[34] R. Gao, D. Yan, Fast formation of single-unit-cell-thick and defect-rich layered double hydroxide nanosheets with highly enhanced oxygen evolution reaction for water splitting, Nano Res. 11 (2018) 1883–1894, https://doi.org/10.1007/s12274-017-1806-x.

[35] G. Liu, R. Yao, Y. Zhao, M. Wang, N. Li, X. Bo, J. Li, C. Zhao, Encapsulation of Ni/Fe_3O_4 heterostructures inside onion-like N-doped carbon nanorods enables synergistic electrocatalysis for water oxidation, Nanoscale 10 (2018) 3997–4002, https://doi.org/10.1039/C7NR09446A.

[36] W. Ye, X. Fang, X. Chen, D. Yang, Three-dimensional nickel-chromium layered double hydroxide Micro/nanosheet array as an efficient and stable bifunctional electrocatalyst for overall water splitting, Nanoscale 10 (2018) 1–3, https://doi.org/10.1039/C8NR05974H.

[37] X. Fang, X. Xiang, S. Ji, D. Yan, Hierarchical hollow nanotubes of NiFeV-layered double hydroxides@CoVP heterostructures towards efficient pH-universal electrocatalytical nitrogen reduction reaction to ammonia, Appl. Catal. B: Environ. 265 (2020) 118559, https://doi.org/10.1016/j.apcatb.2019.118559.

[38] G. Liu, M. Wang, Y. Wu, N. Li, F. Zhao, Q. Zhao, J. Li, 3D porous network heterostructure NiCe@NiFe electrocatalyst for efficient oxygen evolution reaction at large current densities, Appl. Catal. B: Environ. 260 (2020) 118199, https://doi.org/10.1016/j.apcatb.2019.118199.

[39] W. Ye, Y. Yang, X. Fang, M. Arif, X. Chen, D. Yan, 2D cocrystallized metal−Organic nanosheet array as an efficient and stable bifunctional electrocatalyst for overall water splitting, ACS Sustain. Chem. Eng. 7 (2019) 18085, https://doi.org/10.1021/acssuschemeng.9b05126.

[40] R. Gao, H. Zhang, D. Yan, Iron diselenide nanoplatelets: stable and efficient water-electrolysis catalysts, Nano Energy 31 (2017) 90–95, https://doi.org/10.1016/j.nanoen.2016.11.021.

[41] M.W. Louie, A.T. Bell, An investigation of thin-film Ni–Fe oxide catalysts for the electrochemical evolution of oxygen, J. Am. Chem. Soc. 135 (2013) 12329–12337, https://doi.org/10.1021/ja405351s.

[42] Z. Qiu, Y. Ma, T. Edvinssn, In operando Raman investigation of Fe doping influence on catalytic NiO intermediates for enhanced overall water splitting, Nano Energy 66 (2019) 104118, https://doi.org/10.1016/j.nanoen.2019.104118.

[43] R. Gao, D. Yan, Recent development of Ni/Fe-based micro/nanostructures toward photo/electrochemical water oxidation, Adv. Energy Mater. 10 (2020) 1900954, https://doi.org/10.1002/aenm.201900954.
[44] W.D. Zhang, H. Yu, T. Li, Q.T. Hu, Y. Gong, D.Y. Zhang, Y. Liu, Q.T. Fu, H.Y. Zhu, X. Yan, Z.G. Gu, Hierarchical trimetallic layered double hydroxide nanosheets derived from 2D metal-organic frameworks for enhanced oxygen evolution reaction, Appl. Catal. B: Environ. 264 (2020) 118532, https://doi.org/10.1016/j.apcatb.2019.118532.
[45] Z. Zhang, G. Liu, X. Gui, B. Chen, Y. Zhu, Y. Gong, F. Saleem, S. Xi, Y. Du, A. Borgna, Z. Lai, Q. Zhang, B. Li, Y. Zong, Y. Han, L. Gu, H. Zhang, Crystal phase and architecture engineering of lotus-thalamus-shaped Pt-Ni anisotropic superstructures for highly efficient electrochemical hydrogen evolution, Adv. Mater. 30 (2018) 1801741, https://doi.org/10.1002/adma.201801741.